Numerical investigation of thermal buckling and post-buckling behavior of an EN AW 6016-T4 car roof assembled in a steel body-in-white

Leandro M. da Silva, Christophe Cellard, Edouard Geslain, Laurent Sohier, Olivier Ponte-Felgueiras, Romain Créac'Hcadec

▶ **To cite this version:**

Leandro M. da Silva, Christophe Cellard, Edouard Geslain, Laurent Sohier, Olivier Ponte-Felgueiras, et al.. Numerical investigation of thermal buckling and post-buckling behavior of an EN AW 6016-T4 car roof assembled in a steel body-in-white. Mechanics & Industry, 2023, 24, pp.36. 10.1051/meca/2023032 . hal-04250653

HAL Id: hal-04250653
https://hal.science/hal-04250653

Submitted on 19 Oct 2023

HAL is a multi-disciplinary open access archive for the deposit and dissemination of scientific research documents, whether they are published or not. The documents may come from teaching and research institutions in France or abroad, or from public or private research centers.

L'archive ouverte pluridisciplinaire **HAL**, est destinée au dépôt et à la diffusion de documents scientifiques de niveau recherche, publiés ou non, émanant des établissements d'enseignement et de recherche français ou étrangers, des laboratoires publics ou privés.

Mechanics & Industry **24**, 36 (2023)
© L.M. da Silva et al., Published by EDP Sciences 2023
https://doi.org/10.1051/meca/2023032

Mechanics & Industry

Available online at:
www.mechanics-industry.org

REGULAR ARTICLE

OPEN ACCESS

Numerical investigation of thermal buckling and post-buckling behavior of an EN AW 6016-T4 car roof assembled in a steel body-in-white★

Leandro M. da Silva[1,2,*], Christophe Cellard[3], Edouard Geslain[4], Laurent Sohier[3], Olivier Ponte-Felgueiras[1], and Romain Créac'hcadec[2,5]

[1] Stellantis, 35177 Chartres de Bretagne, France
[2] IRDL UMR CNRS 6027, ENSTA-Bretagne, 29806 Brest cedex 9, France
[3] IRDL UMR CNRS 6027, Université de Bretagne Occidentale, 29200 Brest, France
[4] IRDL UMR CNRS 6027, Université de Bretagne Sud, Lorient, France
[5] Excelcar, 35131 Chartres de Bretagne, France

Received: 31 May 2023 / Accepted: 28 August 2023

Abstract. The automotive industry is undergoing significant changes driven by factors such as reducing carbon dioxide emissions, advancing technology, evolving regulations, and the emergence of new energy sources. Lightweight materials, particularly aluminum alloys, are being extensively researched and integrated into vehicles to reduce weight and improve performance. However, the heating process during vehicle production can cause thermal buckling in thin aluminum alloy structures, affecting their appearance and quality. While thermal buckling has been studied in other industries, research in the automotive sector, particularly for non-structural parts like car roofs, is limited. This study uses numerical simulation to predict thermal buckling and post-buckling behavior of a EN AW 6016-T4 alloy car roof assembled in a predominantly steel body-in-white. The research findings indicate that roof buckling occurs at a relatively low temperature difference of approximately 60 °C, which is lower than the maximum temperatures experienced during the painting phases in the automotive industry. Consequently, undulations in the roof's shape become apparent, underscoring the importance of design modifications to ensure visual conformity. Validation through physical testing confirms the model's accuracy, providing valuable insights for designing lightweight structures with improved performance and aesthetics.

Keywords: Automotive industry / aluminum alloy / EN AW 6016-T4 / numerical simulation / thermal buckling

1 Introduction

In the present era, the automotive industry is driven by several factors including the global demand for reduced carbon dioxide emissions, the progress of technology under the concept of Industry 4.0, the evolving international regulations, and the emergence of new energy sources [1–4]. These factors are encouraging extensive research and development within the industry to integrate lightweight materials into future vehicles. As a result, vehicles are increasingly composed of a diverse range of materials, strategically applied to minimize unnecessary weight in specific areas of the cars. In this context, aluminum alloys have gained significant prominence in the transportation industry due to their light weight, durability, recyclability, ductility, corrosion resistance, and strength properties [5,6].

Notwithstanding its potential as a viable approach to minimize the weight of automobiles, the implementation of thin aluminum structures within multi-material assemblies encounters obstacles, specifically pertaining to the heating procedure of the body-in-white throughout the painting stage. This phase involves subjecting the structure to temperatures around 180 °C for durations of several minutes. Such significant temperature fluctuations during vehicle fabrication can lead to the buckling of body-in-white structures. Consequently, this thermal buckling can result in the formation of defects that directly impact the product's shape and appearance. In response to the rapid technological developments and changes, extensive theoretical analyses and experimental investigations have been conducted to address thermal buckling issues. Researchers

★ This paper is sponsored by the conference IDDRG 2022, held in Lorient in June 2022, in relation to the theme "What's up in forming and mechanical joining of sheet metals?".

* e-mail: leandromauricio.silva@outlook.com

This is an Open Access article distributed under the terms of the Creative Commons Attribution License (https://creativecommons.org/licenses/by/4.0), which permits unrestricted use, distribution, and reproduction in any medium, provided the original work is properly cited.

Table 1. Chemical composition of EN AW 6016-T4 studied (wt.%).

Si	Fe	Cu	Mn	Mg	Cr	Zn	Ti	Al
0.92	0.19	0.09	0.07	0.41	0.01	0.00	0.031	Balance

have frequently studied thermal buckling analysis of functionally graded plates [7–10], as well as thermal buckling in structures composed of composite materials [11,12], among other related works. Moreover, in various industrial sectors such as pipeline industry [13,14], aerospace engineering [15,16], oil refineries [17,18], and nuclear engineering [19], the buckling of thin plates caused by thermal loads has garnered significant attention in the design and analysis of engineering structures.

However, thermal buckling research in the automotive industry remains relatively uncommon. Existing studies primarily focus on analyzing structural components such as brake discs and rotors [20–21]. However, during the vehicle manufacturing process, non-structural parts with significant visual impact, such as the aluminum alloy car roof, can experience significant compliance issues due to their thinness and large heat exchange surface area. As a result, the mechanical response of the roof can vary depending on the heating process and structural design until the completion of the production line. Considering the significant cost and complexity associated with conducting multiple full-scale tests on a body-in-white, this research aims at developing a numerical simulation based on the Finite Element Method to highlight the importance of considering and predicting the thermal buckling and post-buckling behavior of a car roof made of aluminum alloy (specifically, the EN AW 6016-T4 alloy) when assembled within a predominantly steel body-in-white.

2 Material: EN AW 6016-T4

Due to safety, design, and assembly considerations, the body-in-white is composed of various materials, with the majority being different types of steel. In most part of the cases, the melting point of steel exceed 1000 °C, which is significantly higher than the maximum temperature reached during automotive painting operations (around 180 °C). Consequently, the mechanical properties of steel will hardly ever demonstrate significant variations within the studied temperature range. However, the same assertion cannot be applied to aluminum alloys, as their melting temperature is approximately 600 °C [22].

The specific component under investigation is the car roof, which will be subjected to testing using the aluminum alloy EN AW 6016-T4, whose chemical composition is presented in Table 1. The EN AW 6016-T4 alloy used in this study was provided by the company *Constellium* and underwent a natural ageing period of 3 months. Its nomenclature follows the standards established by the *Comité Européen de Normalisation* (CEN). This nomenclature indicates that the prefix "EN AW" designates a wrought aluminum alloy [23], and it further implies that the material underwent a heat treatment prior to its arrival at the laboratory for testing: the T4 heat treatment.

The chemical composition of EN AW 6016-T4 renders the material prone to undergo hardening processes characterized by alterations in its microstructure, influenced by both the natural ageing time and the thermal cycles to which the material is exposed [24,25]. More specifically, the present EN AW 6016-T4 sheet contained 0.92% Si and 0.41% Mg as age-hardening elements. Consequently, this phenomenon induces variations in the thermomechanical properties of the alloy, necessitating a comprehensive understanding of its behavior. Therefore, conducting tensile tests under elevated temperature conditions becomes essential for accurate characterization.

3 Experimental procedure

For the performance of the tensile tests, the standards ISO 6892-1:2019 and ISO 6892-2:2018 were used to define the guidelines of the tests at room temperature and at high temperature conditions, respectively. The tests were performed using a universal testing machine INSTRON 5585 with a load cell with a maximum load capacity of 200 kN and an environmental chamber INSTRON 3119-407. The loading rate of the upper crosshead was set as 1.13 mm/min. The specimens used in the experiment had a thickness of 1.10 mm (±0.02 mm) and their geometry is shown in Figure 1A. In order to prevent material transformation caused by high cutting temperatures in other methods such as laser cutting, water jet cutting was employed during the manufacturing process. The strain measurements in this study were performed using Digital Image Correlation (DIC) as the measurement technique, as depicted in Figure 1B. The choice of this technique was based on previous research findings, which have demonstrated the reliability of DIC for strain analysis in tensile tests conducted at temperatures below 650 °C [26–30].

For this study, GOM Correlate Pro software was selected for the analysis and subsequent data treatment. The technique of random speckle patterns on the specimen was used. So, a black–white speckle pattern was sprayed onto the study surface of the samples and, subsequently, the system configuration underwent calibration, facilitated by a precisely dimensioned calibration target measuring 23 × 18 mm.

To carry out the tensile tests, an image that will serve as a reference image is taken just before each test, then images of the specimen are taken during the deformation process until rupture. The stress–strain curve data were acquired at regular 2-second intervals through the association of stress data derived from the tensile testing machine and strain data extracted via the DIC method. The determination of strain involves a process, wherein the software captures displacement measurements within the defined DIC zone. Subsequently, these measurements obtained

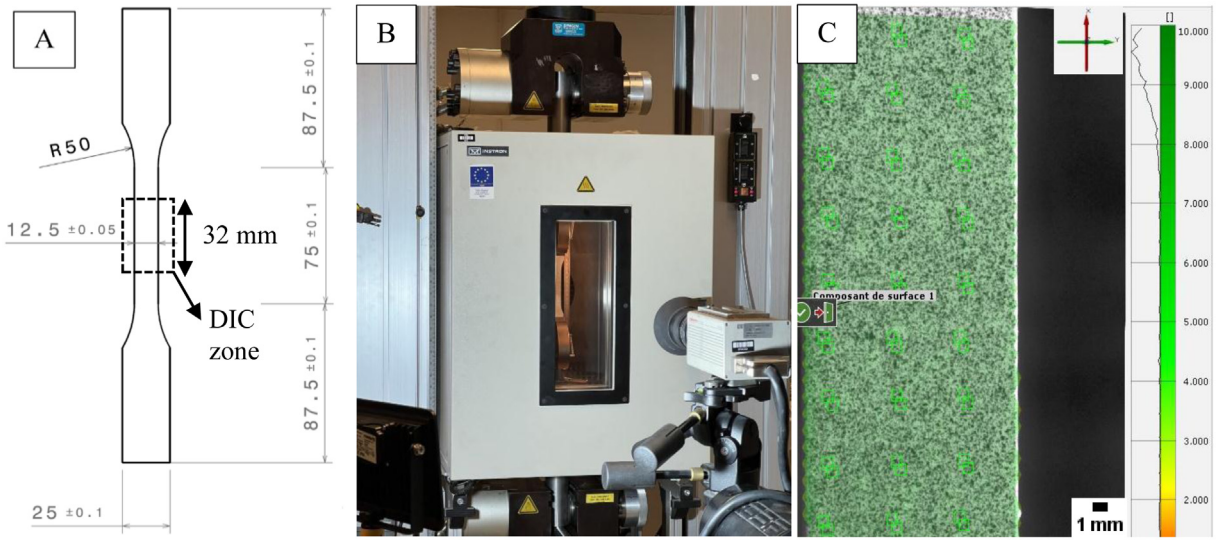

Fig. 1. (A) Geometry of the specimens for tensile tests (units in millimetre). (B) Photo of the assembly for the tensile test. (C) Speckle pattern quality on a scale from zero to ten for a test according to the GOM Correlate Pro software.

from the specified region of interest are used to calculate strain, then they undergo a process of averaging to ascertain accurate and representative strain values.

Knowing that the accuracy and precision in DIC measurements depends also on the quality of the speckle pattern, tests were only taken into account if the speckle patterns were of a considerably good quality according to GOM Correlate software. This analysis of the quality of the speckle pattern executed by GOM Correlate and visually depicted in Figure 1C considers a multitude of critical factors, including pattern size, pattern density, the starkness of contrast achieved between the distinctive speckles and the underlying background, and the meticulous identification of any potential sources of interference or noise—ranging from the influence of shadows to reflections.

In regard to the analysis of stress and strain results, it is well established that aluminum alloys exhibit significant plastic deformation, rendering the properties calculated using the engineering stress (σ_{eng}) and engineering strain (ε_{eng}) not the most suitable. Therefore, in this study, the graphs will be drawn from the true stress (σ_{true}) and the true strain (ε_{true}). Considering the constant volume assumption (the incompressibility assumption), it is possible to calculate the value of the true stress (σ_{true}) as a function of engineering stress and engineering strain:

$$\sigma_{true} = \sigma_{eng}.\left(1 + \varepsilon_{eng}\right). \quad (1)$$

As for the true deformation (ε_{true}), it can be calculated by:

$$\varepsilon_{true} = \ln(1 + \varepsilon_{eng}). \quad (2)$$

Tensile tests covered a temperature range representative of automotive industry production lines, which included tests at room temperature, 140 °C, 180 °C, and 220 °C. To ensure statistical significance of the following results, a minimum of three valid tests were performed at each temperature.

In terms of the analysis of the elastic limit, the $Rp_{0.2}$ (0.2% offset yield strength) of the material exhibited a non-linear increase from 107.67 MPa at room temperature to 161.59 MPa at 220 °C, as shown in Figure 2B and Table 2. This indicates a significant temperature-dependent enhancement in yield strength in a non-linear manner. Examining the average elongation of the material, the results shown in Figure 2A reveal a trend towards decreased ductility at elevated temperatures. This phenomenon can be attributed to the formation of β”-precipitates around 230 °C, which act as barriers impeding dislocation movement. Consequently, while the yield strength is augmented, the ductility is concurrently reduced [31,32]. The presence of these precipitates restricts the plastic deformation mechanisms, limiting the material's ability to elongate before fracture.

The average values obtained for the Young's modulus (E) were calculated from the slope of the elastic part of the curves shown in Figure 2A. As can be seen in Figure 2C, contrary to what occurs with the elastic limit, the values of E decreased in a non-linear way from 65.19 MPa at room temperature to 48.33 MPa at 220 °C. This softening can be explained because with the increase in temperature we begin to approach the melting temperature of the material, which makes the material able to distribute stresses more easily.

Figure 2A also reveals that the stress vs strain curve starts to have a tendency to show slight negative slope in the plastic deformation zone at 220 °C. This fact is due to the formation of Mg- and Si- clusters at around 80 °C, formation of Guinier-Preston zones (GP-zones) at around 150 °C and formation of β”-precipitates at around 230 °C [31,32]. The formation of these precipitates significantly

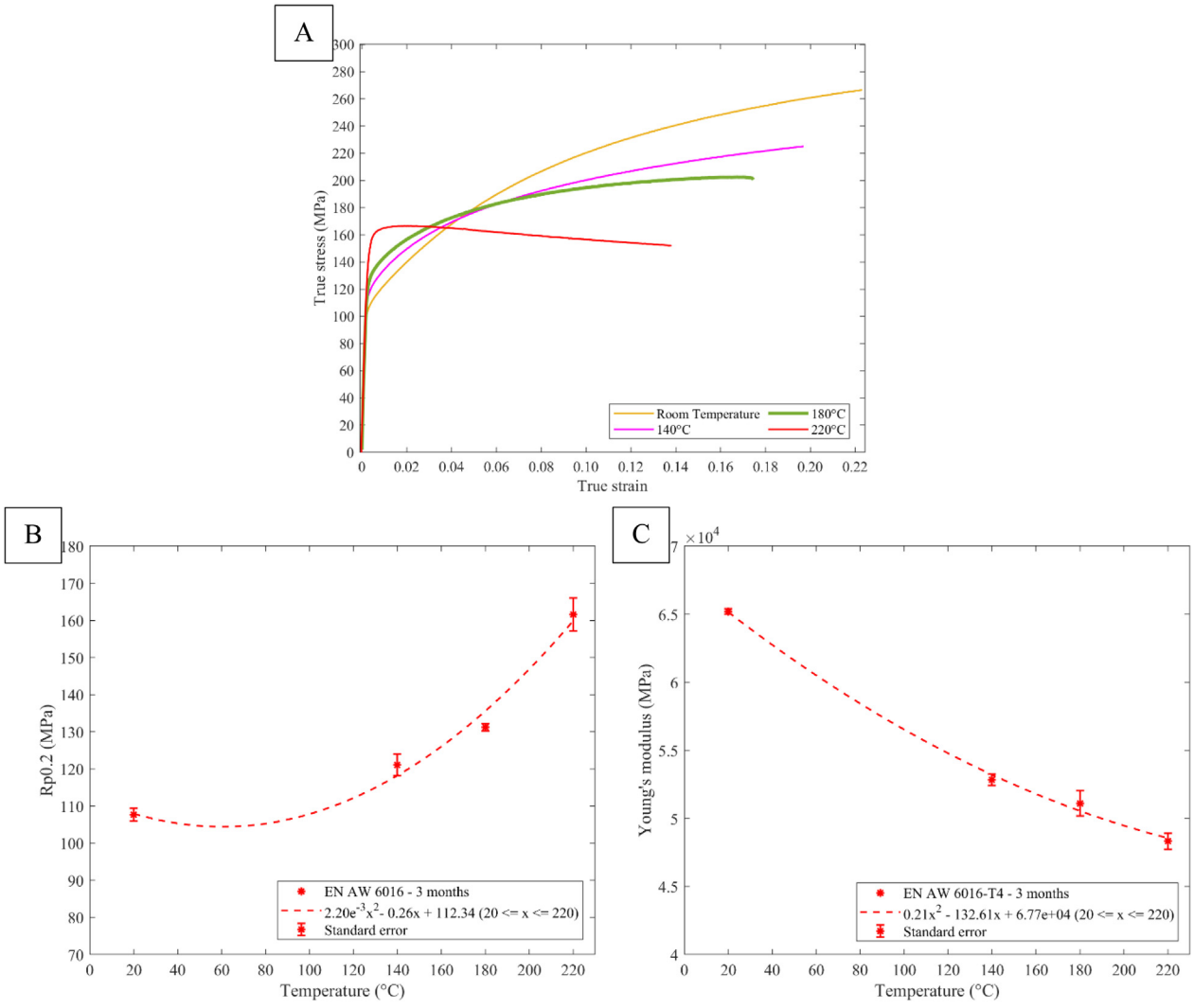

Fig. 2. Results obtained for the EN AW 6016-T4 naturally aged for three months. (A) Average of true stress versus true strain curves for each temperature situation studied. (B) Average evolution of the elastic limit, obtained at the stress level corresponding to a plastic strain of 0.2%, analyzed in relation to temperature. (C) Average evolution of Young's modulus in relation to temperature evolution.

Table 2. Result of the analysis of the mechanical properties. $\overline{\mathbf{R}}\mathbf{p}_{0.2}$ is the average of the elastic limits obtained with an offset of 0.2% from the elastic zone; $\mathbf{SD}(\mathbf{Rp}_{0.2})$ is the standard deviation of the elastic limits; $\mathbf{Error}(\overline{\mathbf{R}}\mathbf{p}_{0.2})$ is the standard error of the elastic limits; $\overline{\mathbf{E}}$ is the average of the Young's moduli; $\mathbf{SD}(\overline{\mathbf{E}})$ is the standard deviation of Young's moduli; $\mathbf{Error}(\overline{\mathbf{E}})$ is the standard error of the Young's moduli; $\overline{\mathbf{R}}\mathbf{p}_{0.2}{}^{0^\circ}$ **and** $\mathbf{Rp}_{0.2}{}^{90^\circ}$ are, respectively, the averages of the elastic limits obtained from the specimens cut at 0° from the rolling direction and at 90°; Similarly, $\overline{\mathbf{E}}^{0^\circ}$ e $\overline{\mathbf{E}}^{90^\circ}$ are the averages of the Young's moduli obtained from specimens cut at 0° from the rolling direction and at 90°.

Temperature (°C)	$\overline{\boldsymbol{Rp}}_{0.2}$ (MPa)	SD$(\overline{\boldsymbol{Rp}}_{0.2})$ (MPa)	Error$(\overline{\boldsymbol{Rp}}_{0.2})$ (MPa)	$\overline{\boldsymbol{E}}$ (GPa)	SD$(\overline{\boldsymbol{E}})$ (GPa)	Error$(\overline{\boldsymbol{E}})$ (GPa)	$\frac{\overline{\boldsymbol{Rp}}_{0.2}{}^{0^\circ}}{\boldsymbol{Rp}_{0.2}{}^{90^\circ}}$	$\frac{\overline{\boldsymbol{E}}^{0^\circ}}{\boldsymbol{E}^{90^\circ}}$
Room Temp.	107.67	4.34	1.77	65.19	0.46	0.19	1.07	1.02
140	121.10	5.05	2.92	52.83	0.70	0.40	1.02	1.00
180	131.21	1.69	0.98	51.11	1.60	0.92	1.02	1.06
220	161.59	8.93	4.47	48.33	1.18	0.59	0.93	0.97

impacts the material's response to mechanical loading due to their distinct influence. Additionally, dislocation creep, which is characteristic of aluminum alloys, begins to take effect around 250 °C [33]. These combined factors contribute to the observed change in the slopes of the stress-strain curves, particularly at elevated temperatures.

In order to find out if the material studied has isotropic or anisotropic behavior in terms of yield strength, the specimens were made and tested in two directions (in the rolling direction and at 90° from the rolling direction). Observing in Table 2, it is possible to see that the results of the proportion between the elastic limit at 0.2% for the samples cut in the rolling direction and at 90° ($\frac{Rp_{0.2}{}^{0^\circ}}{Rp_{0.2}{}^{90^\circ}}$) is between 0.93 and 1.07, which is very close to 1. Consequently, the anisotropy in the yield strength is negligible for this material within the studied temperature range.

The results obtained from this study align with the conclusions drawn in the work of Engler[25]. In that study, an analysis of the EN AW 6016 −T4 alloy was conducted for three distinct in-plane orientations to the rolling direction: 0°, 45°, and 90°. The findings from this examination echo the observation that the sheet material displays minimal in-plane anisotropy. Notably, a slight discrepancy of only 2 MPa exists between the maximum and minimum yield strengths, evident at orientations 0° and 90°.

Similar congruence is evident in the investigations undertaken by Simões et al. [34]. In their study, uniaxial tensile tests were performed across a range of temperatures, spanning from ambient conditions to 300 °C. These experiments employed the Gleeble machine, generating rapid heating within seconds, and encompassed deformation rates from 2×10^{-4} s^{-1} to 2×10^{-2} s^{-1}. The outcomes underscore a parallel observation: uniaxial tensile tests conducted at distinct orientations (0°, 45°, and 90°) relative to the rolling direction consistently reveal the material's negligible anisotropic behavior in terms of yield stresses, regardless of temperature variations.

Furthermore, based on the findings presented in Table 2, a similar observation can be made regarding the analysis of Young's modulus. The calculated ratios ($\frac{\overline{E}^{0^\circ}}{\overline{E}^{90^\circ}}$) range from 0.97 to 1.02, indicating a value close to 1. Hence, the results further support the notion that the Young's modulus remains relatively consistent and unaffected by the angle of orientation.

Another point of note is that, as evidenced from Table 2, the highest standard deviations for the elastic limits and the Young's Modulus are 8.93 MPa and 1.18 GPa, respectively. These values remain considerably minor in comparison to the average values obtained for their respective analyzed properties, thus signifying a robust convergence concerning the results.

After completing the investigation on the temperature-dependent mechanical properties of EN AW 6016-T4, the subsequent stage focuses on predicting the displacement and deformation characteristics of the structure during the heating phase in the paint ovens. This involved conducting an analysis of buckle and post-buckle behavior on the body-in-white structure, utilizing the mechanical properties of the studied material.

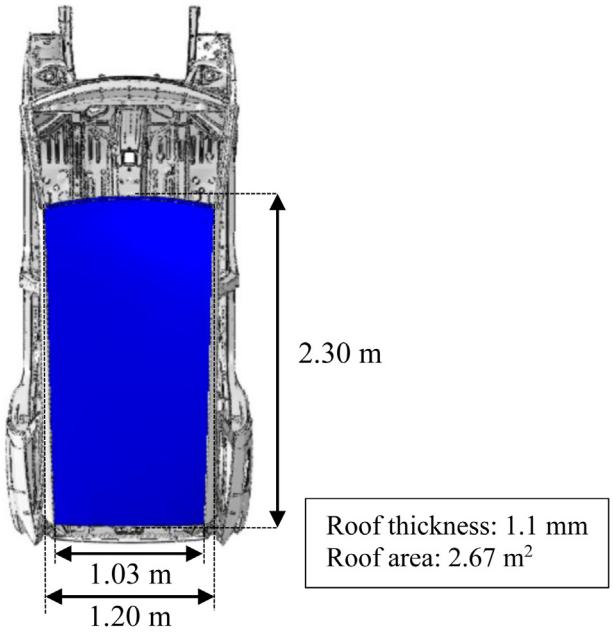

Fig. 3. Structural dimensions of the assembled roof in the body-in-white.

4 Thermal buckle and post-buckle analysis

In this stage of the study, the structural performance of a generic SUV roof (with dimensions shown in Fig. 3) assembled in a body-in-white will be initially evaluated in terms of thermal buckling. The objective of this analysis is to determine whether the configuration of the roof, made of EN AW 6016-T4 material, poses a potential risk of experiencing buckling during the heating process in the painting phase, thereby compromising the structural conformity and visual integrity of the structure.

For a large-scale geometry such as the body-in-white, numerous factors (including a wide variety of materials, different boundary conditions for each component, cost, development time, etc.) make the analytical study of thermal buckling highly complex and big amount of structural tests impractical in terms of cost, time, and understanding of the underlying physical phenomena. Hence, a linear buckling analysis was conducted using the ABAQUS software to study the thermal buckling behavior of the structure. By employing this numerical technique, the complex interaction between temperature and structural response can be evaluated, allowing for a comprehensive understanding of the thermal buckling phenomenon.

The numerical model of the EN AW 6016-T4 incorporates material properties and previously obtained true stress vs true strain curves through the integration of temperature-dependent data. This entails accounting for

variations in the Young's Modulus, yield strength, and elasto-plastic behavior of the material in response to temperature changes. The model employs linear interpolation between data points to establish a continuous representation across temperature ranges. Given the intricate interplay between temperature fluctuations and material response, the endeavor to formulate distinct hardening laws tailored to each temperature scenario is notably complex. As a pragmatic resolution, the methodology of isotropic hardening was embraced. This approach captures the material's dynamic response to diverse thermal conditions using the temperature-dependent curves obtained from the tensile tests, thus preserving model integrity and comprehensibility without undue complexity. This strategic selection aligns harmoniously with the endeavor of modeling the sizable vehicle structure while factoring in the nuances of temperature-induced variations.

In terms of geometry, given that structures subjected to compressive loading can buckle in non-axisymmetric modes, it was chosen to perform the buckling analysis with the complete geometry [35]. From a mathematical perspective, utilizing the notation outlined in the ABAQUS User Guide, the software aims to determine the outcomes of the subsequent equation:

$$K^{MN} v^{M} = 0, \tag{3}$$

where K^{MN} is the tangent stiffness matrix when the loads are applied, and the v^{M} are nontrivial displacement solutions.

Developing equation (3), we arrive at:

$$K_0{}^{NM} + \lambda_i \, {}_{K\Delta}{}^{NM}) v_i{}^{M} = 0 \tag{4}$$

where $K_0{}^{NM}$ is the stiffness matrix corresponding to the base state, which includes the effects of the preloads, λ_i are the load multipliers, also called eigenvalues (for this reason the magnitude of the load is not important, as it will be multiplied by this factor until reaching the solutions of the equation), ${}_{K\Delta}{}^{NM}$ is the differential initial stress and load stiffness matrix due to the incremental loading pattern, $v_i{}^{M}$ are the buckling mode shapes (eigenvectors), N and M refer to degrees of freedom of the whole model and i refers to the ith buckling mode. If we call the preloads P^N and the incremental loading pattern Q^N, the critical buckling loads are then $P^N + \lambda_i Q^N$. This justifies the fact that for Eigen mode analysis there needs to be a disturbance load in the model.

In the case of the studied model, the disturbance load will be the temperature variation that will cause a thermal expansion or contraction of the material. The coefficient of thermal expansion employed for the EN AW 6016-T4 material was $2.25 \times 10^{-5}\,°C^{-1}$. To facilitate the calculations, we choose an initial temperature of 0°C for the model and apply a temperature change of +1 °C. Thus, the results of the eigenvalues given by the simulation will be the buckling temperatures of each mode. Beyond applying the load, ensuring precise boundary conditions stands as a critical factor in achieving an accurate depiction of the buckling phenomenon. Thus, simulating these conditions numerically in close alignment with real-world scenarios becomes imperative.

In this context, the car roof is linked to the body-in-white through spot welding and brazing, as demonstrated in Figure 4A. To aptly encapsulate the essence of these connections within numerical simulations, multiple point constraints (MPC) were employed. These constraints guarantee that the translational and rotational behaviors of the interconnected points remain the same, preventing any relative rotation or translation between the car roof and the body-in-white at these specific junctions.

Figure 4B presents the simulation results of the first eigenvalues for each side of the full-geometry model, employing an S4 mesh for the roof, which are 4-node, stress-displacement shell elements endowed with large-strain formulation. The elements were selected to possess an approximate global size of 5 mm per side. This resulted in an extensive mesh, comprising a total of 111 540 elements solely dedicated to modeling the car roof.

By observing Figure 4B, it can be noted that temperature variations of 56.9 °C and 57.0 °C are required to induce buckling on the right and left sides of the roof, respectively. The close proximity of these temperatures suggests that buckling will occur nearly simultaneously on both sides of the structure. Notably, these temperatures are relatively low compared to the temperature variations encountered during the production process in the automotive industry, typically ranging from 140 °C to 220 °C. Consequently, a post-buckling analysis becomes essential to evaluate the structural behavior beyond the buckling initiation stage.

There exist various numerical methods to simulate the post-buckling behavior of structures. Two common approaches involve applying a load to trigger the activation of buckling modes [36] or imposing displacements at specific locations on the structure [37]. In this research, we adopted a strategy where the buckling mode shapes are employed as geometric imperfections within the model. In this study, the term "imperfections" pertains to deliberate initial deviations from an idealized state, introduced into the model to capture irregularities. This choice was motivated by the inherent presence of initial geometric imperfections in engineering structural elements under real-world conditions. Consequently, the buckling mode shapes obtained from the buckling simulation are going to be used as valuable data for subsequent post-buckling analyses.

On ABAQUS, imperfections have the form of:

$$\Delta x_i = \sum_{i=1}^{k} w_i . \varphi_i, \tag{5}$$

where ϕ_i represents the i^{th} mode shape and w_i is the associated scale factor, k is the number of selected buckling modes to be considered in the post-buckling analysis, and Δx_i denotes the resulting imperfection value [38]. To quantify these inherent deviations, we employed a dial gauge to measure the initial geometric imperfections in a sample cut from the EN AW 6016-T4 aluminum sheet of

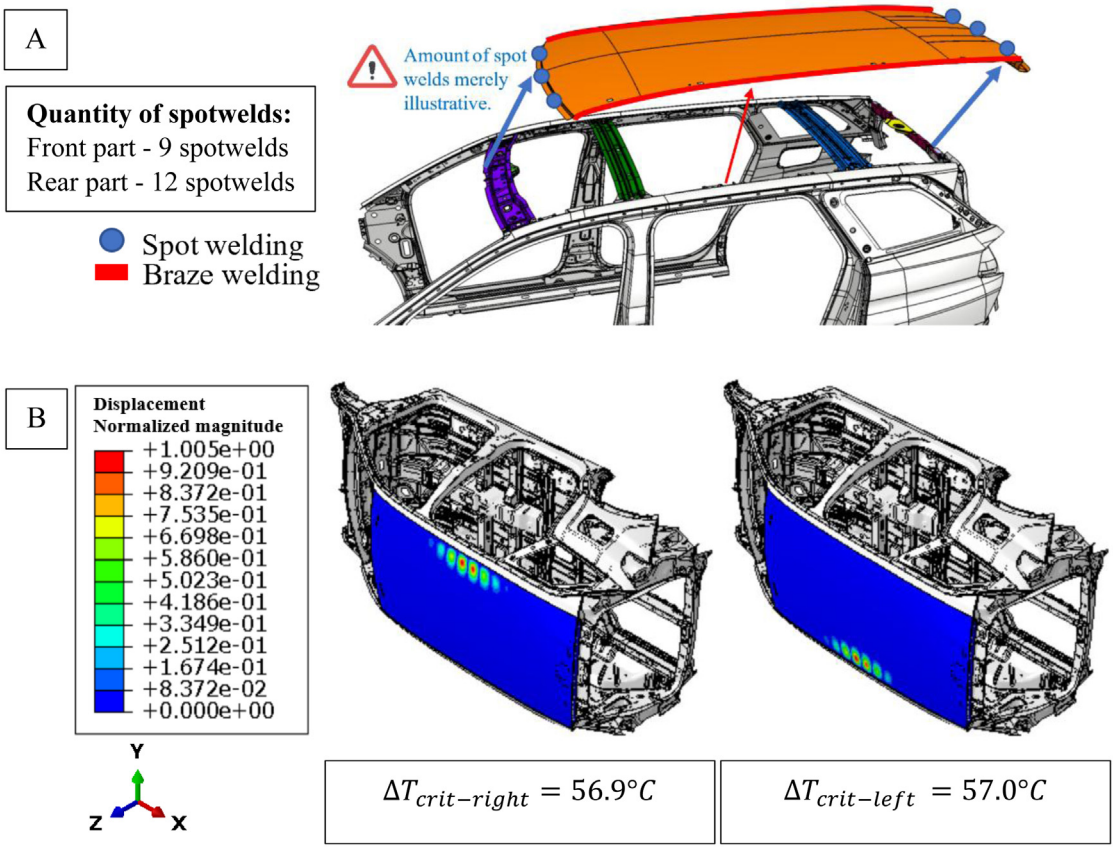

Fig. 4. (A) Boundary conditions related to the assembly of the car roof with the body-in-white. (B) Result of the thermal buckling analysis through Finite Element simulation. $\Delta T_{\text{crit}-\text{right}}$ and $\Delta T_{\text{crit}-\text{left}}$ represent, respectively, the temperature variation required to reach the first buckling mode on the right and left sides of the car roof.

1.1 mm thickness after its production. These imperfections were found to be in the order of 0.01 mm. Thus, a imperfection factor of 0.01 was chosen to the post-buckle simulation.

A temperature curve representing the heating operations in the automotive painting phase was utilized as a thermal load (refer to Fig. 5). Given the relatively large size of the structure, temperature heterogeneities are expected to occur. For industrial simplification purposes, the temperature application is divided into three groups of components: external parts (surrounding the vehicle externally), internal parts (located in the vehicle's interior paint), and intermediate parts (between the external and internal components). Since the thermal loads depicted in Figure 5 are applied gradually over time, the influence of acceleration in the post-buckle phase can be considered negligible. Consequently, an implicit analysis approach is deemed suitable for investigating our problem. Additionally, as post-buckling deformations do not exhibit direct proportionality to the applied loads, the simulation incorporates geometric nonlinearity. Thus, the prior examination of material properties concerning temperature assumes paramount significance.

5 Results and discussion

The determination of the critical buckling temperature can be achieved through the application of the Budiansky criterion [39]. This criterion relies on identifying a sudden change in the curvature of the load-displacement or temperature−displacement response curve. Consequently, Figure 6A showcases the out-of-plane displacement curves derived from the results of post-buckling simulations along a specific line (highlighted by the red line in Fig. 6B), strategically positioned at a distance of 53 mm from the right edge of the roof. This specific location was chosen due to its alignment with the epicenter of the most significant out-of-plane displacements observed within the structure.

As depicted in Figure 6A, the first pronounced change in out-of-plane displacement manifests itself at a temperature of 63.3 °C, exhibiting a peak displacement magnitude occurring between the 1.2-meter and 1.4-meter positions along the length of the car roof. Under the highest temperature condition investigated (green curve in Fig. 6A—180 °C), the Z-directional displacement reaches a maximum value of 8.3 millimeters, while the minimum

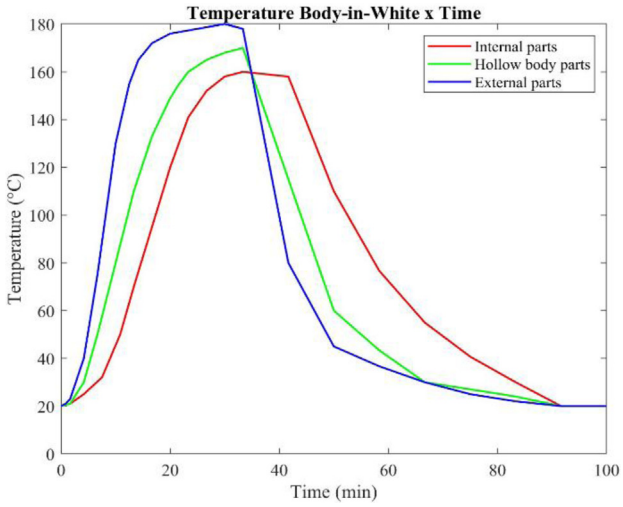

Fig. 5. Temperature graph used in numerical analysis. The structural components are divided into three groups: external parts (surrounding the vehicle externally), internal parts (located in the vehicle's interior), and hollow body parts (between the external and internal components).

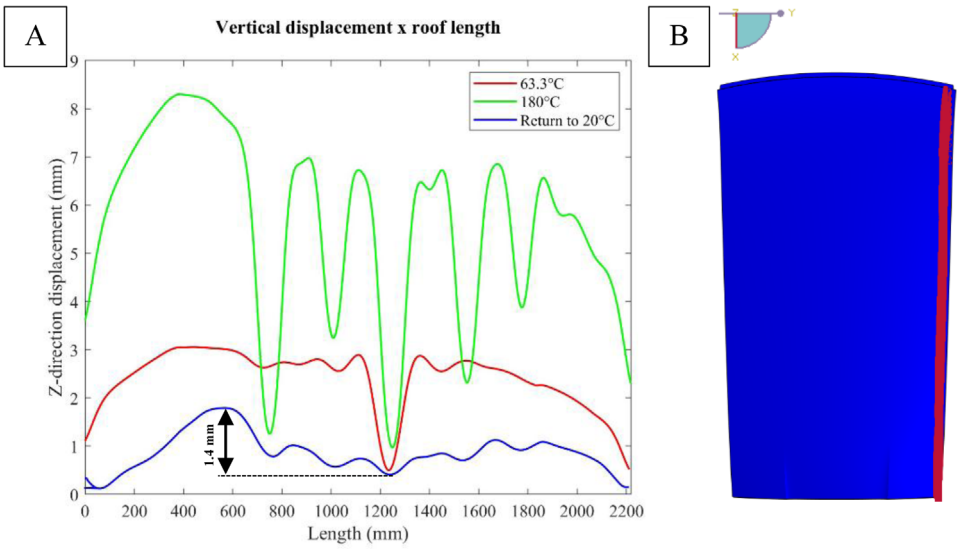

Fig. 6. (A) Evolution of out-of-plane displacement derived from the results of post-buckling simulations along the red line highlighted in 6-B at 63.3 °C, 180.0 °C and upon return to 20 °C. (B) Line at a distance of 53 mm from the right edge of the roof (epicenter of the most significant out-of-plane displacements).

displacement amounts to 1.0 millimeter, resulting in a maximum difference of 7.3 millimeters. Furthermore, the displacement curve as a function of length reveals subtle undulations subsequent to the structure's return to a temperature of 20 °C, with maximum variation of the undulations measuring 1.4 mm, as shown in Figure 6. These undulations can be attributed to the complex interplay between the car roof's response to the heating process and the differential expansion of the body-in-white components. They represent a potential challenge concerning the visual conformity of the structure, as they introduce irregularities and deviations from the desired aesthetic standards.

Figure 7 illustrates the outcomes of the analysis conducted on the z-directional displacement field, plastic deformation patterns, and principal compressive stresses to evaluate the mechanical behavior of the structure at various temperatures. The chosen temperature points

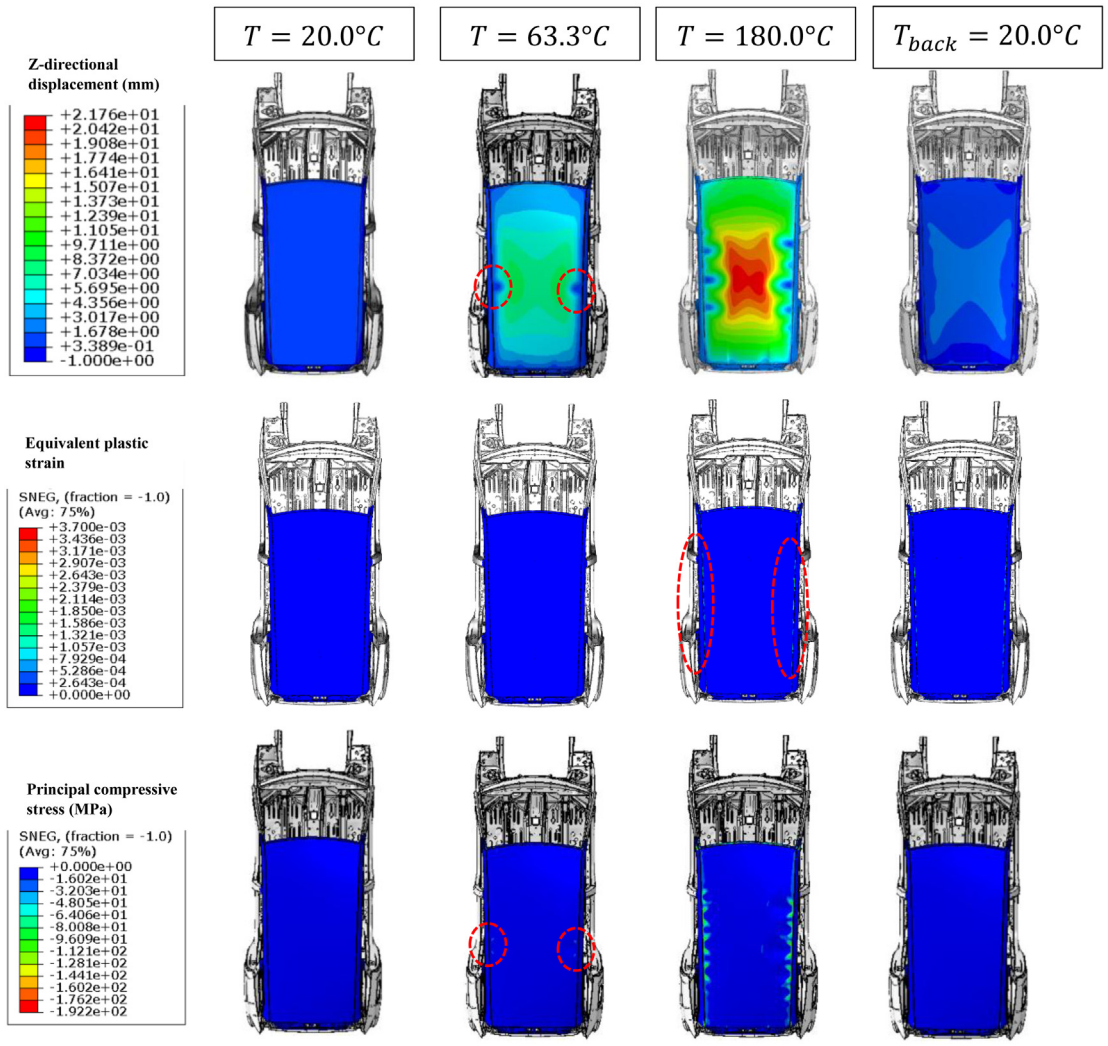

Fig. 7. Body-in-white analysis of Z-directional displacement, equivalent plastic strain, and principal compressive stresses fields at 20 °C, 63.3 °C, 180 °C and return to 20 °C.

included 20 °C, 63.3 °C, 180 °C, and the return to 20 °C. At the initial condition for the post-buckling simulation (20 °C), the structure exhibited stability.

At 63.3 °C, buckling initiation was observed. In Figure 7, the circled red regions in the displacement field and principal compression field indicate the appearance of displacement and stress peaks. This signifies the onset of buckling. Additionally, analyzing the equivalent plastic strain field revealed that the structure experienced buckling while still within the elastic strain domain.

At 180 °C, it was evident from the displacement and stress analyses that the roof had fully buckled. The presence of numerous local peaks in these fields indicated significant displacement variations and the appearance of some plasticity. Notably, in Figure 7, the circled red region at the lateral borders of the roof showed evidence of an equivalent plastic strain of 0.37%. This was a result of the boundary condition imposed to represent the weld line between the roof and the body side of the body-in-white. Moreover, the maximum value of the principal compressive stress at the roof was measured at −140.7 MPa.

The equivalent plastic strain observed at 180 °C caused the structure to remain deformed even after the cooling process back to 20 °C. This deformation resulted in the undulations seen in the analysis of the out-of-plane displacement, as depicted in Figure 7.

In order to validate the final state of the roof, after conducting the numerical analysis of the problem, a real body-in-white with the same design as the simulation was subjected to the same thermal loading as imposed in the simulation. At the end of this process, the structure was taken to a scanning booth, enabling the creation of a point cloud for the virtual reconstruction of the structure. The virtual post-processing analysis was carried out using the Polyworks software. Through this analysis, it was possible to identify the visual defects on the car roof. By comparing

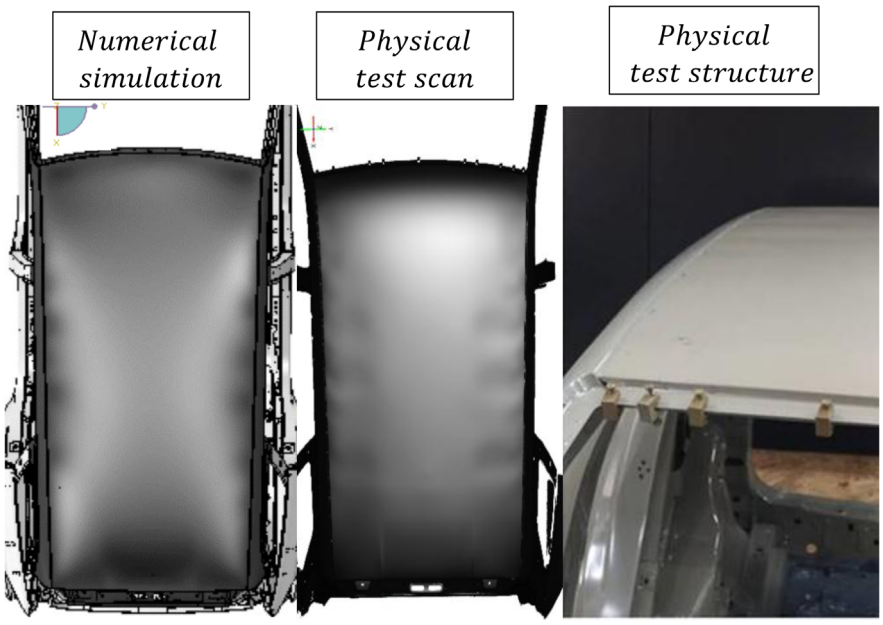

Fig. 8. Comparison of appearance results for the roof: numerical simulation, real structure scan, and photographic analysis (respectively, from left to right).

the results of the physical test with those of the simulation, as presented in Figure 8, a satisfactory correlation is observed in terms of the manner in which the structure buckles and the location of the buckling-induced undulations, which are predominantly found near the lateral edges of the roof. Hence, the visual conformity issues highlighted by the simulation were validated through the physical test.

To establish one more link between numerical simulation and the physical vehicle structure, we utilized Polyworks software to extract relative displacement values between the structure after the heating phase and the structure prior to entering the paint ovens. The outcomes of these relative displacements are visualized in Figure 9. It's important to emphasize that the reference points employed for scanning differ from those used in the numerical simulation. This discrepancy arises due to the intricate production processes involving stamping and assembly that lead to the final real-world structure. Consequently, disparities in absolute displacement values are to be expected between the physical and numerical models.

Despite these disparities, there are consistent variations in the wave amplitudes generated by the post-buckling effect, which can be effectively compared with the simulation results. Upon analyzing the results showcased in Figure 9, a conspicuous pattern emerges: the lateral regions of the car roof exhibit notable shape irregularities, with the most prominent displacement variation observed in the Z-direction within the undulated region, measuring 1.3 mm. This value corresponds closely to the maximum displacement variation of 1.4 mm previously obtained in

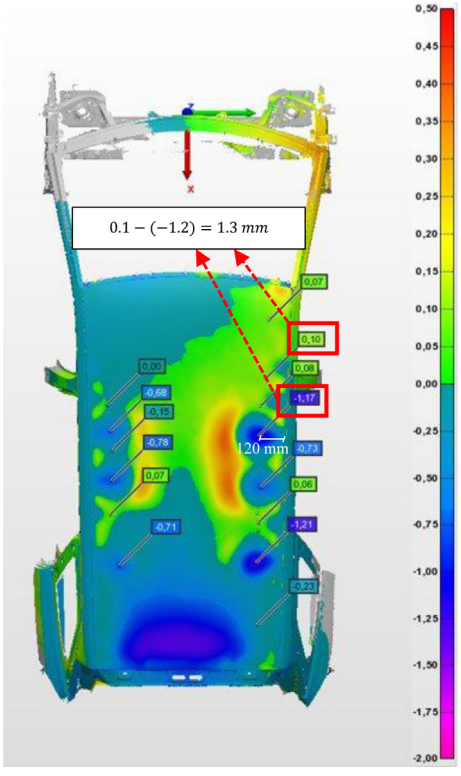

Fig. 9. Relative displacement results between the vehicle before and after heating phase. These results were obtained through the scan conducted with the car roof made of EN AW 6016-T4. Measurements are in millimeters.

the right undulated zone of the roof, as shown in Figure 6A. This agreement substantiates the correlation in terms of displacement magnitude, and it offers compelling evidence of a significant shape defect within this vehicle structure.

6 Conclusion

This study addresses the instability issue faced by the aluminum alloy EN AW 6016-T4 roof structure of an SUV vehicle when assembled with a predominantly steel body. Conducting full-scale tests on the structure is complex in terms of time, cost, and obtaining scientific conclusions. Therefore, a numerical methodology was developed to predict the mechanical behavior of the structure in terms of thermal buckling.

It can be concluded that due to the differential thermal expansion of the various body structures, problems related to roof buckling occur at a temperature difference of approximately 60 °C, while the structure is still within its elastic regime. This temperature variation is relatively small compared to the maximum temperatures experienced by the vehicle during production (180 °C). Hence, accounting for post-buckling behavior is essential to predict the final appearance of the roof in the vehicle. In this research, the consideration of buckling modes for post-buckling simulation was accomplished by introducing imperfections with an amplitude factor of 0.01 into the model.

According to the obtained results, the structure exhibits undulations at the end of the heating phase, with a maximum amplitude of 1.4 mm near the lateral edges of the roof. Such deviations from a smooth and uniform displacement pattern can significantly affect the aesthetic appearance and overall quality of the car roof, which is a critical aspect in automotive design and manufacturing. To validate the numerical model results, a physical test on the full-scale structure was conducted, and the results regarding the shape and location of roof surface defects exhibited similar trends in both cases. Moreover, the maximum displacement variation observed in the out-of-plane direction within the same undulated region was measured 1.3 mm, indicating agreement with the numerical simulation results and compelling evidence of a significant shape defect within the roof structure.

Therefore, this study emphasizes the importance of mitigating these undulations and ensuring the structural integrity and visual conformity of the car roof through design modifications to reinforce the problematic area. This is essential for meeting desired standards of the automotive industry and customer expectations.

Declaration of competing interest

The authors declare that they have no known competing financial interests or personal relationships that could have appeared to influence the work reported in this paper.

Funding

This research was funded by the Association Nationale de la Recherche et de la Technologie (ANRT) and by the funding of the AM2 project carried out by the company Stellantis. This study was also carried out with the support of Institut de Recherche Dupuy de Lôme (IRDL). We gratefully acknowledge the support provided by all these entities.

References

[1] European Council, Paris Agreement on climate change, https://www.consilium.europa.eu/pt/policies/climate-change/paris-agreement/ (accessed March 14, 2023)
[2] European Commission, CO_2 emission performance standards for cars and vans, https://ec.europa.eu/clima/policies/transport/vehicles/regulation_en (accessed March 14, 2023)
[3] The European Parliament and the Council of the European Union, Regulation (EU) 2019/631 of the European Parliament and of the Council of 17 April 2019 setting CO_2 emission performance standards for new passenger cars and for new light commercial vehicles, Off. J. Eur. Union L **111/13** (2019)
[4] S. Vaidyaa, P. Ambad, S. Bhosle, Industry 4.0-a glimpse, Procedia Manuf. **20**, 233–238 (2018)
[5] D. Brough, H. Jouhara, The aluminium industry: a review on state-of-the-art technologies, environmental impacts and possibilities for waste heat recovery, Int. J. Thermofluids **1-2**, 100007 (2020)
[6] R. Zhao, C. Nowicki, L. Gosselin, C. Duchesne, Energy and exergy inventory in aluminum smelter from a thermal integration point-of-view, Int. J. Energy Res. **40**, 1321–1338 (2016)
[7] S.A.M. Ghannadpour, H.R. Ovesy, M. Nassirnia, Buckling analysis of functionally graded plates under thermal loadings using the finite strip method, Comput. Struct. **108–109**, 93–99 (2012)
[8] X. Zhao, Y.Y. Lee, K.M. Liew, Mechanical and thermal buckling analysis of functionally graded plates, Compos. Struct. **90**, 161–171 (2009)
[9] H. Wu, S. Kitipornchai, J. Yang, Thermal buckling and postbuckling of functionallygraded graphene nanocomposite plates, Mater. Des. **132**, 430–431 (2017)
[10] T. Van Do, D.H. Doan, N.D. Duc, T.Q. Bui, Phase-field thermal buckling analysis forcracked functionally graded composite plates considering neutral surface, Compos. Struct. **182**, 542–548 (2017)
[11] D. Wang, J. Hui, W. Cao, Y. Yang, Y. Wan, H. Zuo, B. Zhang, The influence of geometric imperfections on post-buckling behavior and free vibrations of a fiber-reinforced composite laminated plate under thermal loading, Compos. Struct. **306**, 116568 (2022)
[12] G. Manickam, A. Bharath, A.N. Das et al., Thermal buckling behaviour of variable stiffness laminated composite plates, Mater. Today Commun. **16**, 142–51 (2018)
[13] Z.K. Wang, C.G. Soares, Theoretical investigation on the upheaval thermal buckling of a lined subsea pipeline, Ocean Eng. **261**, 111843 (2022)

[14] Z. Wang, C. Guedes Soares, Upheaval thermal buckling of functionally graded subsea pipelines, Appl. Ocean Res. **116**, 102881 (2021)
[15] M.J. Santer, A. Wheatley, Composite tube flexures at nanosatellite scale, AIAA 2017 -0622, Session: small satellite deployable structures, https://doi.org/10.2514/6.2017–0622
[16] W.L. Ko, Thermal buckling analysis of rectangular panels subjected to humped temperature profile heating, NASA Dryden Flight Research Center (2004) NASA/TP-2004–212041, H-2539.Ko.fm (nasa.gov)
[17] Y. Li, J. Jiang, Y. Yu, Z. Wang, Z. Xing, Q. Zhang, Thermal buckling of oil-filled fixed-roof tanks subjected to heat radiation by a burning tank, Eng. Fail. Anal. **138**, 106393 (2022)
[18] R.C. Jaca, L.A. Godoy, H.D. Calabro, S.N. Espinosa, Thermal post-buckling behavior of oil storage tanks under a nearby fire, Int. J. Pres. Ves. Pip. **189**, 104289 (2021)
[19] A. Ghorbanpour Arani, M. Ahmadi, A. Ahmadi, A. Rastgoo, H. A. Sepyani, Buckling analysis of a cylindrical shell, under neutron radiation environment, Nucl. Eng. Des. **242**, 1–6 (2012)
[20] H. Yang, Finite element analysis of thermal buckling in automotive clutch and brake discs, Electronic theses and dissertations, 1056 (2015)
[21] M.H. Pranta, M.S. Rabbi, S.C. Banik, M.G. Hafez, Y.M. Chu, A computational study on structural and thermal behavior of modified disk brake rotors, Alexandria Eng. J. **61**, 1882–1890 (2022)
[22] Materials, Design and Manufacturing for Lightweight Vehicles,. Chapter 3-Aluminum Alloys for Lightweight Automotive Structures.2nd ed., Woodhead Publishing, 2020
[23] European Aluminium Association, The aluminium automotive manual: materials − designation system (2002)
[24] P.J. Bolt, R.J. Werkhoven, A.H. Van den Boogaard, Effect of elevated temperatures on the drawability of aluminium-sheet components, Proceedings 4th Esaform Conference, Liege, 2001
[25] O. Engler, Effect of precipitation state on plastic anisotropy in sheets of the age-hardenable aluminium alloys AA 6016 and AA 7021, Mater. Sci. Eng. A. **830**, 142324 (2022)
[26] M. Quanjin, M. Rejab, Q. Halim, M. Merzuki, M. Darus, Experimental investigation of the tensile test using digital image correlation (DIC) method, Mater. Today.: Proc. **27**, 757–763 (2020)
[27] M. Rund, R. Procházka, P. Konopík, J. Džugan, H. Folgar, Investigation of sample-size influence on tensile test results at different strain rates, Procedia. Eng. **114**, 410–415 (2015)
[28] Y.H. Wang et al., Whole field sheet-metal tensile test using digital image correlation, Exp. Tech. **34**, 54–59 (2010)
[29] J.S. Lyons, J. Liu, M.A. Sutton, High-temperature deformation measurements using digital image correlation, Exp. Mech. **36**, 64–70 (1996)
[30] L. Yu, B. Pan, Overview of high-temperature deformation measurement using digital image correlation, Exp. Mech. **61**, 1121–1142 (2021)
[31] M. Saga, Y. Sasaki, M. Kikuchi, Z. Yan, M. Matsuo, Effect of pre-aging temperature on the behavior in the early stage of aging at high temperature for Al-Mg-Si alloy, Mater. Sci. Forum **217–222**, 821–826 (1996)
[32] G.A. Edwards, K. Stiller, G.L. Dunlop, M.J. Couper, The precipitation sequence in Al-Mg-Si alloys, Acta Mater. **46**, 3893–3904 (1998)
[33] G.S. Wang, K. Liu, S,L, Wang, Evolution of elevated-temperature strength and creep resistance during multi-step heat treatments in Al-Mn-Mg alloy, Materials **11**, 1158 (2018)
[34] V. Simões, H. Laurent, M. Oliveira, L. Menezes, Influence of temperature, strain-rate and aging on the mechanical behaviour of an Al-Mg-Si alloy, 22ème Congrès Français de Mécanique, Lyon, 2015
[35] 6.2.3 Eigenvalue buckling prediction, SIMULIA, http://130.149.89.49: 2080/v6.14/books/usb/default.htm?startat=pt03ch06s02at02.html (accessed February 24, 2023)
[36] A. Humer, A.S. Pechstein, Exact solutions for the buckling and postbuckling of a shear-deformable cantilever subjected to a follower force, Acta Mech. **230**, 3889–3907 (2019)
[37] S.G.P. Castro, E.L. Jansen, Displacement-based formulation of Koiter's method: application to multi-modal post-buckling finite element analysis of plates, Thin-Walled Struct. **159**, 107217 (2021)
[38] 11.3.1 Introducing a geometric imperfection into a model. SIMULIA, https://classes.engineering.wustl.edu/2009/spring/mase5513/abaqus/docs/v6.6/books/usb/default.htm?startat=pt04ch11s03aus55.html(accessed February 24, 2023)
[39] M. Shariyat, Thermal buckling analysis of rectangular composite plates with temperature-dependent properties based on a layerwise theory, Thin Walled Struct. **45**, 439–452 (2007)

Cite this article as: L.M. da Silva, C. Cellard, E. Geslain, L. Sohier, O. Ponte-Felgueiras, R. Créac'hcadec,, Numerical investigation of thermal buckling and post-buckling behavior of an EN AW 6016-T4 car roof assembled in a steel body-in-white, Mechanics & Industry 24, 36 (2023)